

A toolbox of anti-mouse and anti-rabbit IgG secondary nanobodies

Tino Pleiner,¹ Mark Bates,² and Dirk Görlich¹

¹Department of Cellular Logistics and ²Department of NanoBiophotonics, Max Planck Institute for Biophysical Chemistry, Göttingen, Germany

Polyclonal anti-immunoglobulin G (anti-IgG) secondary antibodies are essential tools for many molecular biology techniques and diagnostic tests. Their animal-based production is, however, a major ethical problem. Here, we introduce a sustainable alternative, namely nanobodies against all mouse IgG subclasses and rabbit IgG. They can be produced at large scale in *Escherichia coli* and could thus make secondary antibody production in animals obsolete. Their recombinant nature allows fusion with affinity tags or reporter enzymes as well as efficient maleimide chemistry for fluorophore coupling. We demonstrate their superior performance in Western blotting, in both peroxidase- and fluorophore-linked form. Their site-specific labeling with multiple fluorophores creates bright imaging reagents for confocal and superresolution microscopy with much smaller label displacement than traditional secondary antibodies. They also enable simpler and faster immunostaining protocols, and allow multitarget localization with primary IgGs from the same species and of the same class.

Introduction

Mouse and rabbit antibodies are fundamental tools for numerous basic research techniques and medical diagnostic assays. The detection or immobilization of these primary antibodies is most often performed indirectly via polyclonal anti-IgG secondary antibodies. The need for a continuous supply of anti-IgG sera requires keeping, immunizing, bleeding, and eventually killing large numbers of goats, sheep, rabbits, and donkeys, which is not only costly but also a major animal welfare and ethical problem (Shen, 2013; Reardon, 2016). Furthermore, every new batch of serum contains another heterogeneous mixture of antibodies, which need to be affinity-purified on IgG columns and then depleted (by preadsorption) of nonspecific and cross-reacting antibodies. Moreover, the success of this procedure has to be laboriously quality controlled each time. The large size of secondary antibodies (~10–15 nm; 150 kD) is also a disadvantage, because it limits tissue penetration and introduces considerable label displacement, reducing the obtainable image resolution by superresolution fluorescence microscopy methods (Ries et al., 2012; Szymborska et al., 2013; Pleiner et al., 2015). Their nonrecombinant nature further precludes genetic engineering (tagging or fusion to reporter enzymes).

Why then, have recombinant anti-IgG detection reagents not replaced polyclonal secondary antibodies? The major issue is signal strength. The signal in traditional immunofluorescence, for example, is amplified by (a) multiple secondary IgG molecules binding to distinct epitopes of a primary antibody; (b) a large IgG tolerating many labels per molecule; and

(c) their bivalent binding mode exploiting avidity for high-affinity target recognition. In light of these facts, it appears very challenging to achieve comparable signal levels with a small, monovalent, monoclonal reagent.

We considered nanobodies, single-domain antibodies derived from camelid heavy-chain antibodies (Hamers-Casterman et al., 1993; Arbabi Ghahroudi et al., 1997; Muyldermans, 2013), as perhaps the best candidates for such reagents. Because of their small size (~3 × 4 nm; 13 kD), the possibility of their renewable production as recombinant fusion proteins, and favorable biophysical properties, nanobodies attracted considerable attention as powerful tools in cell biology (Helma et al., 2015) and structural biology (Desmyter et al., 2015), and as future therapeutic agents (Van Bockstaele et al., 2009; Kijanka et al., 2015). They are particularly useful for superresolution imaging (Ries et al., 2012; Szymborska et al., 2013; Pleiner et al., 2015; Göttfert et al., 2017; Traenkle and Rothbauer, 2017). The resolving power of some of the best microscopes reported to date (e.g., ~6 nm by Balzarotti et al. [2017]; ~10–20 nm by Xu et al. [2012] or Huang et al. [2016]) may be reduced as a result of the offset between fluorescent label and target introduced by primary and secondary antibodies (20–30 nm). Site-specifically labeled nanobodies represent a promising solution to this problem, because they can place fluorophores closer than 2 nm to their antigen and, despite their small size, even tolerate up to three dyes (Pleiner et al., 2015).

In this study, we describe the generation of a comprehensive toolbox of nanobodies against all mouse IgG subclasses and rabbit IgG. This work required very extensive optimizations of

Correspondence to Dirk Görlich: goerlich@mpibpc.mpg.de; Tino Pleiner: tino.pleiner@mpibpc.mpg.de; Mark Bates: mark.bates@mpibpc.mpg.de

T. Pleiner's present address is Division of Biology and Biological Engineering, California Institute of Technology, Pasadena, CA.

© 2018 Pleiner et al. This article is available under a Creative Commons License (Attribution 4.0 International, as described at <https://creativecommons.org/licenses/by/4.0/>).



a Overview of all selected anti-IgG nanobodies

Nb ID	CDR III	Subclass specificity	Epitope	Species specificity
TP896	GKFPVESRRHGGTAQWDEYDY	N/A	Fab	Rabbit
TP897	LVFGGEY	N/A	Fc	Rabbit, Gp, Hs (weak)
TP1170	TYSGNYYSNYTVANYGT	Kappa (κ)	Fab	Mouse
TP975	GSQPAFRLSGGSWSRPGDGS	Kappa (κ)	Fab	Mouse
TP1014	RGSSDYDVAMQGEHYTY	Lambda (λ)	Fab	Mouse, Rat, Rabbit (weak)
TP1107	GWWRLPDPDLV	IgG1	Fc	Mouse, Rat, Hs (weak)
TP878	CPGDTYSTICNSDGMIDY	IgG1	Fc	Mouse
TP879	AQFFNDGHQYCPNPY	IgG1	Fc	Mouse, Rat
TP1104	WVLVGREV	IgG1	Fc	Mouse
TP881	GAVRLVAGALRPAD	IgG1	Fc	Mouse, Rat (weak)
TP882	YRRSGAYCTSGGQDY	IgG1	Fc	Mouse, Rat
TP883	AVTYASCNEYDY	IgG1	Fc	Mouse, Rat, Hs (weak)
TP884	GGSDTATSRAY	IgG1	Fc	Mouse, Rat (weak)
TP894	FEQKNYCSGYSLTSLARGVMDH	IgG1	Fc	Mouse
TP895	VARGTWTGRGVDRTTQAMCIPRDPVSDF	IgG1	Fc	Mouse
TP885	VPGYSDYRQGYDY	IgG1	Hinge (?)	Mouse, Rat
TP886	EVTYYSGYTYLFGTKQEYDY	IgG1 (κ+λ)	Fab	Mouse
TP887	QMKFQITMDSYDY	IgG1/2a (κ)	Fab	Mouse
TP888	IFHREITVPRKYDY	IgG1/2a (κ)	Fab	Mouse
TP889	STMRSIDFYVTFDGS	IgG1/2a (κ)	Fab	Mouse
TP890	TFKWEVTTTPDGYDY	IgG1/2a (κ)	Fab	Mouse
TP1106	AVVRQWPNHAQGYDY	IgG1/2a/2b (κ)	Fab	Mouse
TP1129	NKGPHYSDYFDSNLYDF	IgG2a	Fc	Mouse
TP922	EGWEDTITEEPNDENY	IgG2a	Fc	Mouse
TP923	EEGGT	IgG2a	Fc	Mouse
TP926	CARCFVPRMTSAAAYGY	IgG2a	Hinge (?)	Mouse
TP925	VRLSRGYLCRNYDMY	IgG2a/2b	Fc	Mouse
TP979	GVGDGSSCPDSAYEYAY	IgG2b	Fab	Mouse, Gp
TP984	LQSWGSYPHDDY	IgG2b	Fab	Mouse
TP924	GGAATVGGPYDY	IgG3	Fc	Mouse, Rabbit
TP929	LERATMCPRPDTWYDY	IgG2a/3	Fc	Mouse, Rabbit (weak)

Rabbit IgG Nbs; Mouse IgG Nbs specific for: IgG1, IgG2a, IgG2b, IgG3

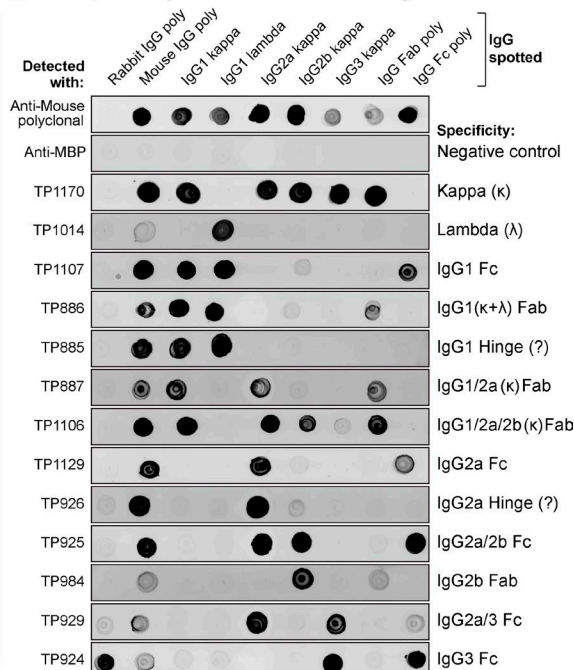
b All specificity classes of anti-mouse IgG nanobodies

Figure 1. Characterization of the anti-IgG nanobody toolbox. (a) Overview of all identified anti-IgG nanobodies. The nanobodies obtained were characterized for IgG subclass and light chain specificity, epitope location on Fab or Fc fragment, and species cross reactivity. The protein sequences of all anti-IgG nanobodies can be found in Table S1. Nb, nanobody; CDR III, complementarity-determining region III; Gp, guinea pig; Hs, human; κ, κ light chain; λ, lambda light chain; Fab, fragment antigen-binding, Fc, fragment crystallizable. **(b)** IgG subclass reactivity profiling of selected anti-mouse IgG nanobodies representing all identified specificity groups. The indicated IgG species were spotted on nitrocellulose strips, and the strips were blocked with 4% (wt/vol) milk in 1× PBS. Then 300 nM of the indicated tagged nanobodies were added in milk. After washing with 1× PBS, bound nanobodies were detected using a fluorescence scanner. Note that the signal strength on polyclonal IgG depends on the relative abundance of the specific subclass (e.g., IgG2b and IgG3 are low abundance) or light chain (κ/λ ratio = 99:1). TP885 and TP926 showed no detectable binding to polyclonal Fab or Fc fragment and might bind to the hinge region. MBP, maltose binding protein; poly, polyclonal.

our routine nanobody selection efforts, such as a time-stretched and thus affinity-enhancing immunization scheme, subsequent affinity maturation including off-rate selections, as well as testing and improving ~200 initial candidates. When labeled site-specifically with fluorophores, the resulting nanobodies performed remarkably well in Western blotting and immunofluorescence. In contrast to polyclonal secondary antibodies, they even allow single-step multicolor labeling and colocalization. In stochastic optical reconstruction microscopy (STORM; Rust et al., 2006) of microtubules, an anti-mouse κ light chain nanobody showed greatly reduced fluorophore offset distances, suggesting its use as a superior alternative to traditional anti-mouse secondary antibodies. Moreover, we show that anti-IgG nanobodies can be conjugated to HRP or expressed as fusions to ascorbate peroxidase (APEX2; Lam et al., 2015) and thus used for enhanced chemiluminescence Western blotting, colorimetric ELISAs, or immuno-EM detection. These monoclonal recombinant nanobodies are thus perfect substitutes for conventional animal-derived polyclonal secondary antibodies. We envision that they can be engineered to enable a more versatile use of the plethora of existing antibodies and even allow the development of more sophisticated antibody-based diagnostic tests.

Results

A comprehensive anti-IgG nanobody toolbox

We immunized two alpacas separately with polyclonal mouse or rabbit IgG and used chemically biotinylated mouse mAbs

of defined subclasses as well as rabbit IgGs for phage display selections of nanobodies from the resulting immune libraries. First results with the initially obtained anti-IgG nanobodies were rather disappointing: we experienced dim and noisy signals in immunofluorescence as well as in Western blots. We reasoned that an increase in affinity and specificity might yield improved reagents, and therefore we reimmunized the animals after a 1-y pause. For this, we used IgGs prebound to multivalent particulate antigens expected to provide strong T-helper cell epitopes. Moreover, we increased the stringency of the subsequent phage display selections by lowering the bait concentration down to the femtomolar range, which should not only select per se for sub-nanomolar binders, but also bring displayed nanobodies in direct competition with each other, because the number of bait molecules was up to 1,000-fold lower than the number of displaying phages. Finally, we performed in vitro affinity maturation by random mutagenesis and further rounds of phage display, this time also combined with off-rate selections. In this way, we obtained a large toolkit of anti-rabbit and anti-mouse IgG nanobodies (Fig. 1 a).

All nanobodies were extensively characterized for subclass specificity, epitope location on Fab or Fc fragment, and cross reactivity to IgGs from other species (Figs. 1 b and S1 a). Their full protein sequences are listed in Table S1, and plasmids for the bacterial expression of selected nanobodies will also be distributed by Addgene (IDs 104157–104164). Notably, we identified nanobodies against all four mouse IgG subclasses and the sole rabbit IgG subclass. Strikingly, many anti-mouse IgG nanobodies target IgG1, which represents the most abundant

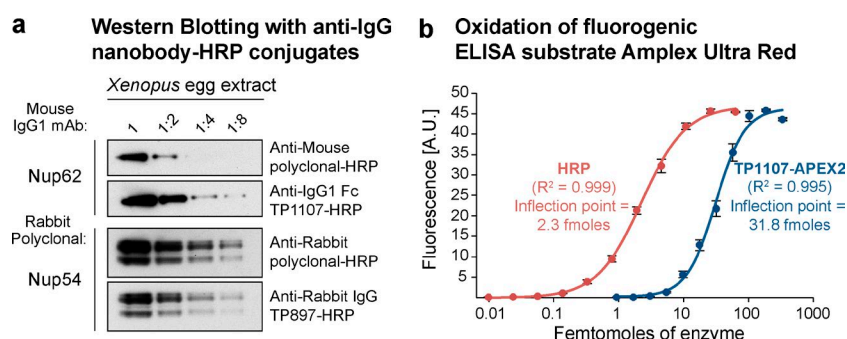


Figure 2. Application of peroxidase-linked anti-IgG nanobodies. (a) A twofold dilution series of *Xenopus* egg extract was blotted and probed with anti-Nup62 mouse IgG1 mAb A225. It was then decorated with HRP-conjugated goat anti-mouse polyclonal IgG (5 nM) or anti-mouse IgG1 Fc nanobody TP1107 (5 nM) and detected via ECL. Similarly, a rabbit polyclonal antibody targeting Nup54 was decorated with HRP-conjugated goat anti-rabbit polyclonal IgG or anti-rabbit IgG nanobody TP897 (5 nM). (b) Oxidation of the fluorogenic ELISA substrate Amplex Ultra Red. A dilution series of pure HRP or recombinant anti-mouse IgG1 Fc nanobody TP1107-APEX2 fusion was incubated with Amplex Ultra Red and H_2O_2 . Oxidation leads to formation of the fluorescent compound resorufin. The data obtained were fit with a four-parameter logistic regression. The inflection points of the curves can be used to compare attainable sensitivity. A.U., arbitrary units. Error bars, mean \pm SD ($n = 3$).

subclass of commercially available mouse mAbs (~62–64%), followed by IgG2a (~22–24%), and the less frequent IgG2b (~13%) and IgG3 (~1–2%). Because the vast majority (~99%) of mouse mAbs possess a κ light chain, anti- κ chain nanobodies promised to be the most broadly useful tools, and we therefore actively selected for such binders by swapping the IgG heavy chain subclass during sequential selection rounds. For the identification of binders targeting the rare λ chain, we had to predeplete the nanobody immune library of heavy chain and κ chain binders. Some of the identified nanobodies have mixed specificities, e.g., multiple mouse Fab-binders target an interface between κ light chain and IgG1 or IgG2a heavy chain. Most anti-mouse IgG nanobodies are exclusively mouse specific, whereas some additionally cross react with rat IgG (Fig. S1 a). The anti-rabbit IgG nanobody TP897 also efficiently recognizes guinea pig IgG. All nanobodies were produced by cytoplasmic expression in *Escherichia coli*, mostly with an N-terminal His-NEDD8-tag for purification by Ni(II) chelate affinity capture and proteolytic release (Frey and Görlich, 2014). They were further equipped with ectopic cysteines for subsequent maleimide labeling reactions (Pleiner et al., 2015). Without further optimization, we typically obtained yields of 15 mg/l of bacterial culture, which already suffices for a million immunofluorescence stains or 200 liters of Western blotting solution.

We first assessed whether the anti-IgG nanobodies were specific and could purify their IgG target from its common source. Anti-rabbit IgG nanobodies TP896 and TP897 isolated polyclonal rabbit IgG from crude rabbit serum with high specificity (Fig. S1 b). Likewise, anti-mouse IgG nanobodies TP881 and TP885 could purify an IgG1 mAb from hybridoma cell culture supernatant (Fig. S1 c). Notably, nanobody-bound IgG was released under physiological conditions using SUMOStar protease cleavage (Pleiner et al., 2015). The main virtue of this approach is perhaps not to purify IgGs from sera, but rather to perform immune-affinity purifications of antigens or antigen complexes that have been prebound to the primary antibodies. In contrast to traditional IPs, this approach makes it possible to release the purified complexes under fully native conditions.

Western blotting with HRP-conjugated anti-IgG nanobodies

We next tested the performance of anti-IgG nanobodies as detection reagents in Western blotting, which is a major application for secondary antibodies. A popular mode of signal detection in Western blotting is ECL, in which antibody-HRP

conjugates are used. HRP is a heme-containing enzyme that catalyzes the oxidation of luminol in the presence of H_2O_2 to yield bright chemiluminescence, which is greatly increased by phenol-derived enhancers. We conjugated maleimide-activated HRP to anti-mouse IgG1 Fc nanobody TP1107 via a C-terminal cysteine (Fig. S2 a) and used the resulting conjugate in ECL Western blotting. The nanobody-HRP conjugate is functional and outperformed a polyclonal secondary antibody-HRP conjugate from a commercial supplier (Fig. 2 a). The anti-rabbit IgG nanobody TP897 could also be linked to HRP, and the resulting conjugate was functional and specific. Uncropped blots are shown in Fig. S2 b. Both TP1107 and TP897 also performed better than two poorly characterized commercially available anti-IgG nanobodies (Fig. S2 c).

Recombinant APEX2 fusion to anti-IgG nanobodies

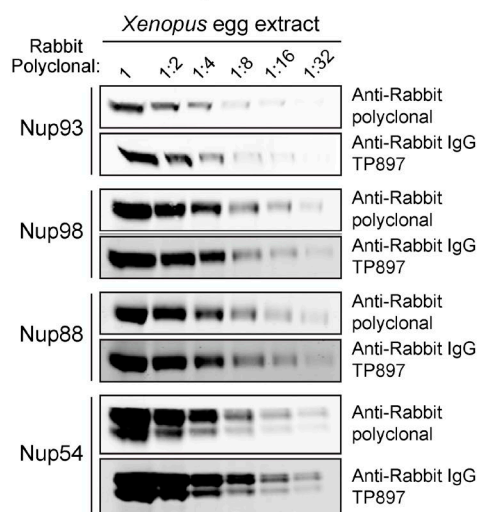
Because of its stability and the breadth of its catalyzed colorimetric or chemiluminescent reactions that allow strong signal amplification, HRP is the preferred enzyme for conjugation to secondary antibodies. However, it still has to be isolated from horseradish roots as a mixture of different isoforms, cannot be made on a practical scale and with a useful specific activity in *E. coli* (Krainer and Glieder, 2015), and fails entirely as a genetic fusion to bacterially expressed nanobodies.

As an alternative, we tested the engineered APEX2 (Martell et al., 2012; Lam et al., 2015) as a fusion partner of the anti-mouse IgG1 Fc nanobody TP1107. The TP1107-APEX2 fusion was not only well expressed and soluble in *E. coli* (Fig. S2 d), but it was also active and efficiently catalyzed the oxidation of the initially colorless substrate Amplex Ultra Red to the highly fluorescent resorufin (Fig. 2 b). In line with previous studies (Lam et al., 2015), HRP seemed slightly more efficient than APEX2 in catalyzing this reaction. Nonetheless, low femtomolar amounts of TP1107-APEX2 could be detected, suggesting its applicability, for instance, in ELISA assays as well as in immunohistochemistry and enzymatic antigen localization in immuno-EM applications.

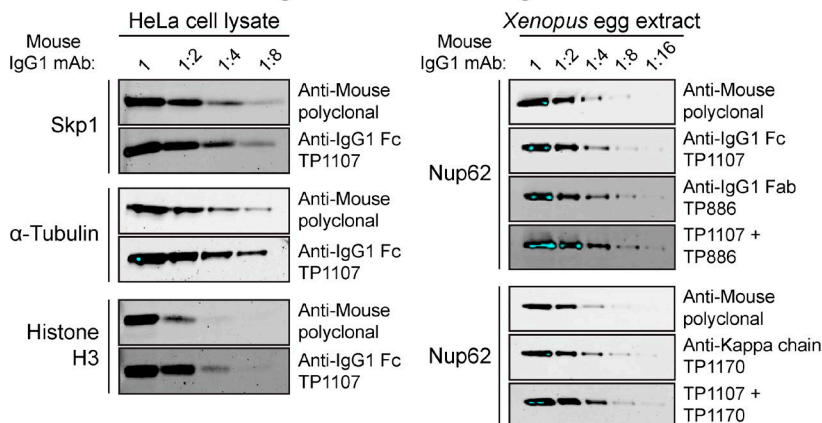
Western blotting with infrared fluorophore-linked anti-IgG nanobodies

A convenient alternative to peroxidase conjugation or fusion is the labeling of secondary antibodies with infrared fluorescent dyes. In fact, infrared fluorescent Western blotting has emerged as a superior alternative to classical ECL. It offers high signal-

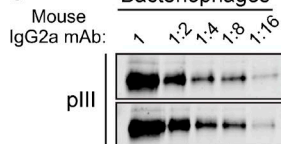
a Western Blotting with anti-rabbit IgG nanobodies



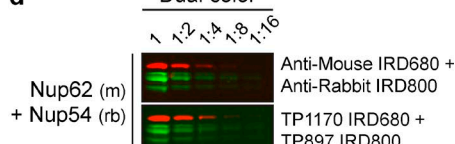
b Western Blotting with anti-mouse IgG nanobodies



c Bacteriophages



d Dual color



to-noise ratios, allows straightforward quantification because of signal linearity over many orders of magnitude, and even enables the simultaneous dual-color detection of multiple proteins. We thus labeled anti-IgG nanobodies site-specifically with the infrared fluorophore IRDye 800 at a C-terminal cysteine (Pleiner et al., 2015). The anti-rabbit IgG nanobody TP897 alone performed just as well as a commercial polyclonal anti-rabbit IgG secondary antibody when it was used with rabbit polyclonal antibodies to detect various nucleoporins (Nups) in a *Xenopus laevis* egg extract (Fig. 3 a). Similarly, the anti-mouse IgG1 Fc-specific nanobody TP1107 gave signal intensities comparable to or even higher than a polyclonal anti-mouse IgG secondary antibody in Western blotting on HeLa cell lysate (Fig. 3 b). Combinations of TP1107 with the compatible anti-mouse IgG1 Fab-specific nanobody TP886 or the anti-mouse κ chain nanobody TP1170 provided clearly better detection sensitivity than the polyclonal secondary antibody. TP1170 allows sensitive detection of IgG2a subclass mAbs, as shown here for the detection of the bacteriophage minor

coat protein pIII (Fig. 3 c). Uncropped Western blots are shown in Fig. S3. We routinely found infrared fluorophore-labeled anti-IgG nanobodies to yield higher detection sensitivity than their HRP-conjugated counterparts. When combined with the compatible IRDye 680, dual-color blots using, for example, mouse and rabbit primary antibodies are easily possible (Fig. 3 d). In contrast to polyclonal secondary antibodies, IRDye-labeled anti-IgG nanobodies give a clean and strong signal when prebound to primary antibodies before application. This makes a separate incubation with the secondary antibody dispensable and saves up to 2 h of processing time per blot. We explored such a one-step staining strategy in more detail for immunofluorescence (see section Rapid one-step immunostaining and colocalization).

Single- and multicolor imaging with anti-IgG nanobodies

We next sought to assess the performance of the anti-IgG nanobodies as detection reagents in conventional indirect

immunofluorescence. For this, cells are incubated sequentially with primary and secondary antibodies with intervening washing steps. Fluorophore-linked polyclonal secondary antibodies are routinely used for detection, because they can bind primary antibodies at multiple sites and thus deliver many fluorophores to enable large signal amplification. In contrast, individual anti-IgG nanobodies target only a single epitope per antibody (or two for symmetric binding sites), and we therefore expected only modest signal amplification.

Strikingly, however, the anti-IgG1 nanobodies TP886 and TP1107, which specifically target IgG1 Fab and Fc fragment, respectively, not only performed well in Western blotting, but also were well-behaved imaging reagents. For maximum brightness, we labeled these nanobodies with two to three fluorophores each at defined cysteines (Pleiner et al., 2015) and used them individually for the detection of mouse IgG1 mAbs in indirect HeLa cell immunostaining (Fig. 4 a). Surprisingly, both were only slightly dimmer than the polyclonal mixture of anti-mouse secondary antibodies. We assume that the excellent nanobody signal is also attributable to less steric hindrance compared with the much larger conventional secondary antibody. When both nanobodies were used in combination, we detected increased signal strengths that often were directly comparable to those obtained with the secondary antibody (e.g., for Vimentin or Ki-67; see also Fig. S4 a). Importantly, despite a high labeling density with (the always somewhat sticky) fluorophores, we observed no detectable background staining with these anti-IgG nanobodies. This probably relates to the fact that the affinity of our nanobodies is very high, which allows their use at rather low nanomolar concentrations. The poor performance of the first anti-IgG nanobody generation indeed suggests that such an excellent signal-to-noise ratio is not a trivial feature for a monovalent detection reagent.

For the detection of IgG2a subclass mAbs, we used a combination of two nanobodies, TP1129 and TP1170 (Figs. 4 b and S4 b). The IgG2a-specific nanobody TP1129 targets an epitope on the Fc fragment and was obtained after affinity maturation of a lower-affinity precursor (Fig. S4 c). Likewise, the κ chain-specific nanobody TP1170 is an affinity-optimized variant, obtained after error-prone PCR, DNA shuffling, and affinity selection (Fig. S4 d). TP1170 also proved effective in combination with the anti-IgG1 Fc nanobody TP1107 for the detection of IgG1 κ mAbs (Fig. S4, e and f). The anti-rabbit IgG Fc nanobody TP897 can be used for the detection of polyclonal and monoclonal rabbit IgG (Fig. 4 c).

The nanobodies presented are specific for their respective IgG subclass, as shown in the specificity profiling dot blot assay (Fig. 1 b). We exploited this for multicolor imaging of HeLa cells with different IgG subclasses (Fig. 4 d). Mouse IgG1-, mouse IgG2a-, and rabbit IgG-specific nanobodies did not show any cross reaction and consequently allowed for clean colocalization experiments. Even triple colocalizations were readily possible.

Rapid one-step immunostaining and colocalization

The main reasons for separate incubation steps of primary and secondary IgGs in indirect immunofluorescence and Western blotting are the large size, as well as the bivalent and polyclonal nature, of conventional secondary antibodies. If primary and secondary antibodies are preincubated, large oligomeric complexes form, which in immunofluorescence cannot easily

penetrate into cells to reach their target and thus create background and poor signal (Fig. 5 a). In contrast, anti-IgG nanobodies are monovalent and therefore do not cross-link primary antibodies. This allows streamlining of the conventional immunostaining procedure to a single step. The primary antibodies are simply preincubated with fluorescently labeled anti-IgG nanobodies and applied to cells together. After washing, the cells can be directly mounted for imaging.

In such a workflow, anti-IgG nanobodies perform exceptionally well (Fig. 5 a). This time-saving protocol is also suitable for colocalization studies combining mouse and rabbit IgGs or combining mouse mAbs of different subclasses. If the off-rate of the IgG prebound nanobodies were negligible over the staining period, then an exchange between the different preformed complexes would also be negligible. This would also make it unnecessary to use different IgG subclasses for multicolor imaging. We thus tested a multicolor staining workflow of HeLa cells, relying solely on IgG1 subclass mAbs (Fig. 5 b). For this, we labeled anti-IgG1 Fc nanobody TP1107 with Alexa Fluor 488, Alexa Fluor 568, or Alexa Fluor 647 maleimide and preincubated it with different IgG1 mAbs. The separately preincubated mixes were then combined and applied to HeLa cells for staining in one step. Strikingly, we obtained clean dual and even triple colocalizations. To preclude an intermixing of colors, unlabeled TP1107 can be added in excess to the final mix, and cells can be postfixed after staining and washing.

Superresolution microscopy with anti-IgG nanobodies

Superresolution fluorescence imaging techniques offer the potential for observing subcellular structures at very small (e.g., nanometer) scales (Bates et al., 2008; Huang et al., 2010; Sahl et al., 2017). However, these methods present new challenges for fluorescent labeling, because the spatial resolution of the images is comparable to the physical size of the probes. In the case of conventional antibodies, the antibody size is on the order of 10–15 nm, which may lead to a significant offset distance between the fluorophore and the epitope. This offset may complicate the interpretation of superresolution fluorescence image data and make it impossible to take full advantage of the increased resolution of the microscope.

Therefore, we reasoned that anti-Fab fragment or anti- κ light chain nanobodies should be ideal imaging reagents for superresolution microscopy, as they would enable small label displacement when used in conjunction with conventional primary antibodies. This would be essentially comparable to using directly labeled Fab fragments of primary antibodies, without any extra work. To test this, we imaged microtubules of BS-C-1 cells using a STORM microscope (Rust et al., 2006; Bates et al., 2007; Fig. 6). Bound primary antibodies were detected either via Alexa Fluor 647-labeled polyclonal anti-mouse secondary antibodies or anti-mouse κ chain nanobody TP1170, and the resulting STORM images had a resolution of ~20 nm. We selected straight regions of microtubule filaments in the images, and calculated the summed histogram of the localizations along the axis orthogonal to the filament axis. Fitting a Gaussian function to each histogram yielded a measure of the filament width. The distribution of widths measured for the two samples is shown in Fig. 6 b. In line with our initial expectations, we observed a striking difference in the microtubules' apparent width for the two images. Microtubules stained via the polyclonal secondary antibody showed

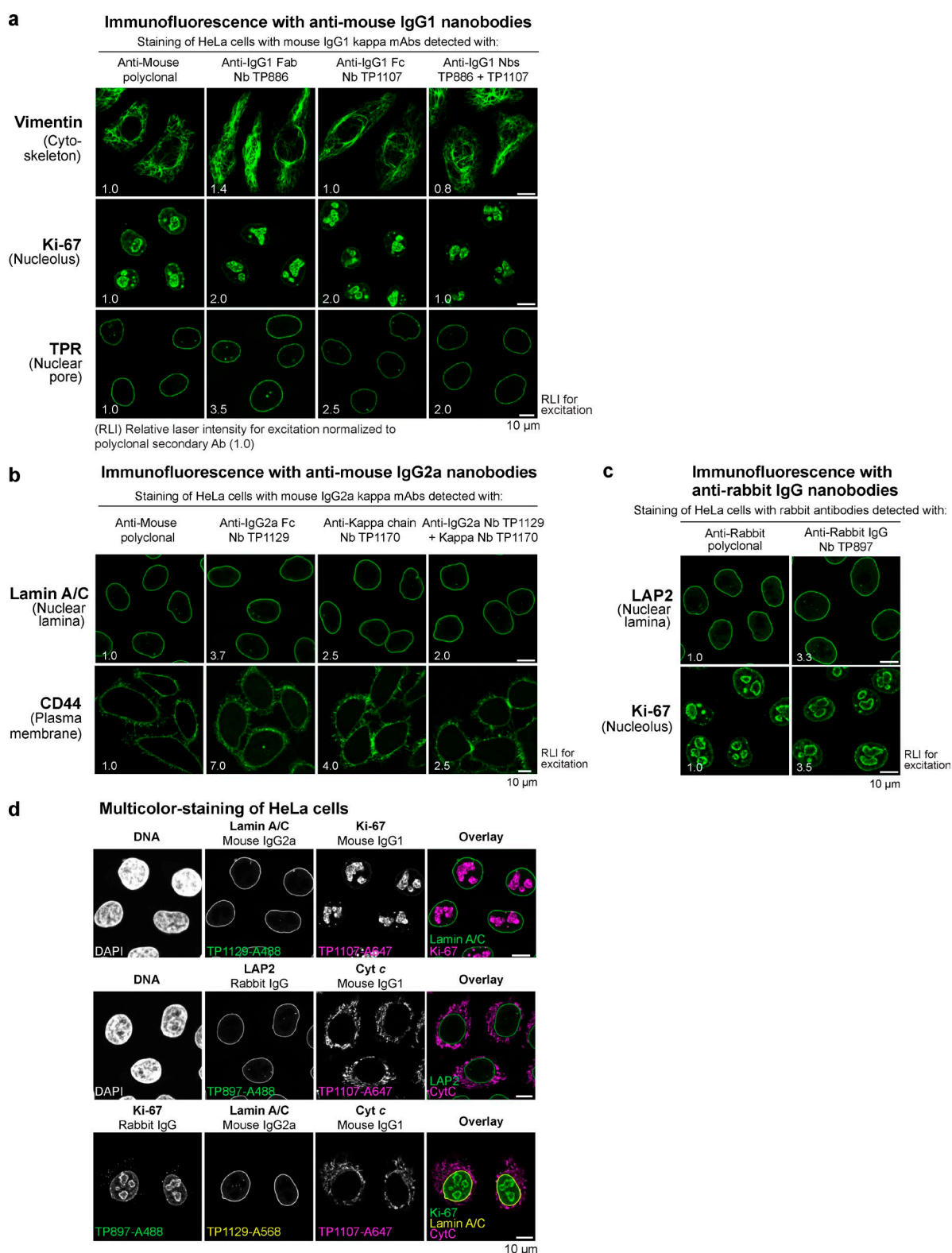


Figure 4. **Imaging with anti-IgG nanobodies.** (a) Immunofluorescence with anti-mouse IgG1 nanobodies. HeLa cells were stained with the indicated mouse IgG1 κ mAbs. These primary antibodies were then detected with Alexa Fluor 488-labeled goat anti-mouse polyclonal antibody, anti-mouse IgG1 Fab nanobody TP886, or anti-mouse IgG1 Fc nanobody TP1107. A combination of TP886 and TP1107 yielded increased staining intensities. Laser intensities used to acquire the anti-IgG nanobody images were normalized to the intensity used to acquire the anti-mouse polyclonal antibody image (RLI, relative laser intensity used for excitation under otherwise identical settings serves as a measure of fluorescence signal strength). (b) Immunofluorescence with anti-mouse IgG2a nanobodies. HeLa cells were stained with the indicated mouse IgG2a mAbs. These primary antibodies were then detected with Alexa Fluor 488-labeled goat anti-mouse polyclonal antibody, anti-mouse IgG2a Fc nanobody TP1129, or anti- κ chain nanobody TP1170. A combination of TP1129 and TP1170 yielded increased staining intensities. (c) Immunofluorescence with anti-rabbit IgG nanobody TP897. HeLa cells were stained with the indicated rabbit antibodies. These primary antibodies were then detected with Alexa Fluor 488-labeled goat anti-rabbit polyclonal antibody

a median width of ~59.5 nm, which is in good agreement with EM studies of antibody-coated microtubules (Weber et al., 1978) and previous STORM imaging (Bates et al., 2007). In contrast, staining with the anti- κ chain nanobody yielded microtubules with a width of 37.5 nm, a remarkable ~22-nm reduction as a result of much lower label displacement compared with the polyclonal secondary antibody.

This result demonstrates, therefore, not only the significant offsets between epitope and fluorophore that may arise in conventional indirect immunostaining, but also the advantage of the smaller nanobody probe. Detection via the anti- κ chain nanobody resulted in an image that more closely reflects the actual structure of the sample, suggesting its use as a superior secondary antibody for any superresolution microscopy involving primary mouse antibodies.

Discussion

Because of the absence of more sustainable alternatives in the past, the great usefulness of polyclonal secondary antibodies in basic research certainly justified their animal-based production. However, to guarantee their constant supply to an ever-growing market, the producing companies had to dramatically increase their livestock, aim for very high antibody titers using aggressive hyperimmunization strategies causing strong side effects, and increase the frequency and volume of collected bleedings. It is therefore not surprising that the industrial scale production of antibodies has led to severe animal welfare and ethical problems. The magnitude of these problems recently surfaced in the Santa Cruz Biotechnology scandal (Shen, 2013; Reardon, 2016).

Ideally, one could replace all animal immunization by selecting binders from synthetic libraries (Gray et al., 2016; Moutel et al., 2016; McMahon et al., 2017; Zimmermann et al., 2017). Yet, with a purely synthetic approach, it is still not straightforward to obtain high-affinity binders. Further, the synthetic strategy is typically also inferior in terms of binder specificity, because it lacks the stringent selection against self-reactivity that happens in antigen-exposed animals. The requirement for specificity is particularly high for secondary antibodies. We therefore see the approach applied here of using an immune library for binder selection as the best possible compromise. Because it is generally sufficient to obtain a few good nanobodies out of a small blood sample containing ~100 million lymphocytes, and because we found methods to further improve the initial candidates *in vitro*, there was no need for any hyperimmunization aiming at high titers. Importantly, once ideal nanobodies are identified, they are defined by their sequence and can be renewably produced in *E. coli* at constant quality and without further animal involvement. Because polyclonal secondary antibody production accounts for the largest share of immunized animals in the world, the anti-IgG nanobodies described in this study have the potential to make a great step forward toward reducing animal use and further contribute to a future of standardized recombinant antibodies (Marx, 2013; Bradbury and Plückthun, 2015a,b).

We expect that our anti-IgG nanobodies will replace polyclonal secondary antibodies in many of their applications, for instance, in Western blotting and immunofluorescence. For both applications, their site-specific and quantitative modification with fluorophores via maleimide chemistry creates superior reagents with predictable label density and position (Pleiner et al., 2015). Furthermore, the precise targeting of primary mouse antibodies at the κ chain with a specific nanobody can substantially reduce label displacement in superresolution microscopy. In the future, we will also explore the direct coupling of anti-IgG nanobodies with engineered cysteines onto colloidal gold particles for electron microscopy, which also suffers from the large linkage error introduced by bulky secondary antibodies.

Because of their monovalent and monoclonal nature, anti-IgG nanobodies do not cross-link primary antibodies, and we exploited this for a one-step immunostaining workflow that saves valuable hands-on time and can also be extended to Western blotting. We envision that for routine stainings, preformed complexes of primary antibodies and labeled nanobodies can be prepared as stock solutions or simply bought from commercial suppliers. Because of the high affinity of the nanobodies described, the same strategy also enables multicolor immunostainings based on a single IgG subclass, which could also be relevant for flow cytometry sorting of specific cell types. This would be a cheaper and more flexible alternative to differentially labeled primary antibodies, it does not pose the risk of inactivating an antigen-binding site, and it can easily be done if only small amounts of primary antibody are available.

Further, because the DNA sequences of these anti-IgG nanobodies are essentially synthetic building blocks, they can be genetically appended to the multitude of available tags, fluorescent proteins, or enzymes to generate fusion proteins with novel functions for tailored applications in basic research and medical diagnostics, and also can become valuable tools for immunology to study Fc or B cell receptors and downstream signaling cascades. Furthermore, anti-IgG nanobodies equipped with protease-cleavable affinity tags (Pleiner et al., 2015) will allow the native isolation of any antibody–target complex, e.g., for structural studies by cryo-EM or functional assays.

Even though the anti-IgG nanobody toolbox presented here is already highly optimized, we will continue to extend it by identifying new nanobodies that decorate complementary binding sites and thus allow further signal enhancement and combining them with additional functional elements. In any case, it will be an open resource for all interested laboratories.

Materials and methods

Alpaca immunization

Two female alpacas, held at the Max Planck Institute for Biophysical Chemistry, were immunized four times with 1.0 mg polyclonal mouse or rabbit IgG at 3-wk intervals. The anti-IgG project turned out to be the most challenging nanobody project in the laboratory so far, because we aimed at an extremely low off-rate for imaging and blotting applications. We therefore resumed immunizations after a 12-mo (rabbit

or anti-rabbit IgG nanobody TP897. **(d)** Multicolor staining of HeLa cells. HeLa cells were incubated with the indicated mouse IgG1, mouse IgG2a, or rabbit IgG antibodies. These primary antibodies were detected via anti-mouse IgG1 Fc nanobody TP1107, anti-mouse IgG2a Fc nanobody TP1129, or anti-rabbit IgG nanobody TP897, respectively, labeled with the indicated Alexa Fluor dyes. The top two panels show dual colocalization, and the bottom panel shows a triple colocalization.

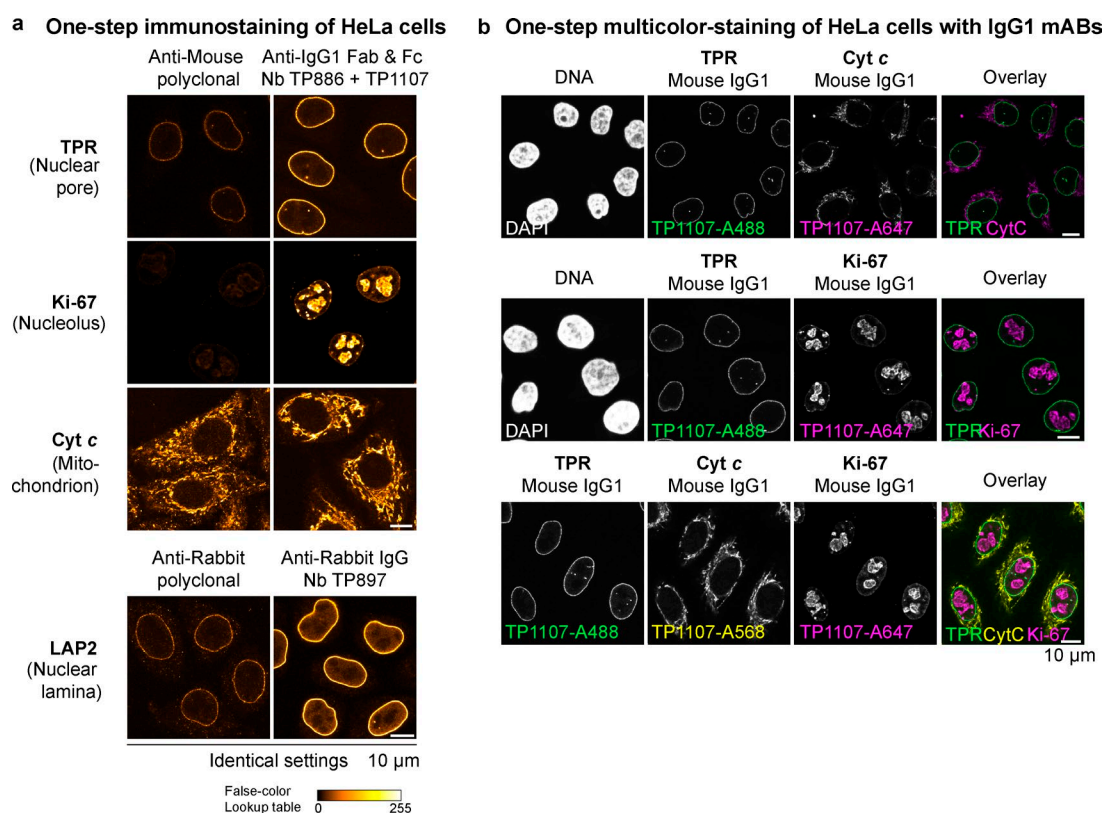


Figure 5. One-step immunostaining of HeLa cells with anti-IgG nanobodies. (a) The indicated mouse IgG1 mAbs were preincubated with an equal amount of Alexa Fluor 488-labeled goat anti-mouse secondary antibody or a combination of anti-mouse IgG1 Fab nanobody TP886 and anti-mouse IgG1 Fc nanobody TP1107. Likewise, the anti-LAP2 rabbit polyclonal antibody was preincubated with either Alexa Fluor 488-labeled goat anti-rabbit secondary antibody or anti-rabbit IgG nanobody TP897. The resulting mixes were then applied to fixed and blocked HeLa cells. After washing, the cells were directly mounted for imaging. For every primary antibody, images were acquired under identical settings, and pixel intensities are represented via a false-color lookup table. (b) Multicolor staining of HeLa cells with mouse IgG1 subclass mAbs. The indicated mouse IgG1 mAbs were separately preincubated with Alexa Fluor 488-, Alexa Fluor 568-, or Alexa Fluor 647-coupled anti-mouse IgG1 Fc nanobody TP1107 and then mixed before staining HeLa cells in a single step. Washed cells were directly mounted for imaging.

IgG) or 8-mo (mouse IgG) break. Nanobodies obtained after these late immunizations still showed very clear phage enrichment (>1,000-fold) even with femtomolar concentrations of the IgG baits. We therefore assume that they have very high affinity.

Selection of anti-IgG nanobodies

The generation of nanobody immune libraries and the selection of antigen-specific nanobodies by phage display from these libraries were performed as previously described (Pleiner et al., 2015). IgG was biotinylated at accessible lysines by addition of a 4 \times molar excess of NHS-PEG₁₂-biotin (from a 20-mM stock in dimethylformamide; Iris Biotech) for 2 h at room temperature in 1 \times PBS. The reaction was quenched, and the excess of unreacted biotin was separated from biotinylated IgG via buffer exchange into 50 mM Tris/HCl, pH 7.5, and 300 mM NaCl using PD-10 desalting columns (GE Healthcare).

Expression and purification of untagged nanobodies

Bacterial expression plasmids for selected anti-IgG nanobodies will be distributed via Addgene under the IDs 104157–104164. The protein sequences of all nanobodies are listed in Table S1. Nanobodies with engineered cysteines were expressed in the cytoplasm of *E. coli* NEB express F' (New England Biolabs). A 50-ml preculture (2YT medium containing 50 μ g/ml kanamycin) was grown overnight at 28°C. The culture was then diluted with fresh medium to 250 ml. After 1 h of growth at 25°C, protein expression was induced for 3–5 h by adding 0.2 mM IPTG. After addition of 1 mM PMSF to

the culture, bacteria were harvested by centrifugation, resuspended in lysis buffer (50 mM Tris/HCl, pH 7.5, 300 mM NaCl, 10 mM imidazole, and 5 mM DTT), and lysed by sonication. The lysate was cleared by ultracentrifugation for 1.5 h (T647.5 rotor, 38,000 rpm; Sorvall) at 4°C. Nanobodies with engineered cysteines carried an N-terminal His₁₄-bdNEDD8-tag and were affinity-purified via Ni²⁺ chelate affinity chromatography. After washing with two column volumes (CV) of lysis buffer and one CV of maleimide-labeling buffer (MLB: 100 mM potassium phosphate, pH 7.5, 150 mM NaCl, and 250 mM sucrose), untagged nanobodies were eluted by on-column cleavage with 500 nM untagged bdNEDP1 protease (expression construct pDG02583; Addgene ID 104129; see section Expression of bdNEDP1 protease from pDG02583; Frey and Görlich, 2014) in maleimide-labeling buffer for 45 min at 4°C and labeled immediately with fluorophores.

Alternatively, nanobodies can be eluted with lysis buffer containing 500 mM imidazole and after buffer exchange to MLB (plus 10 mM imidazole) using PD-10 desalting columns cleaved for 1 h at 4°C in solution with 300 nM His₁₄-MBP-bdSUMO-tagged bdNEDP1 protease. The His₁₄-bdNEDD8 tag and the His₁₄-tagged protease can then be removed by another incubation with Ni²⁺ chelate affinity resin (reverse nickel chromatography). The unbound fraction will contain untagged nanobodies. For longer storage, 10 mM DTT or TCEP and 1 mM EDTA were included in the maleimide-labeling buffer to keep cysteines reduced. Purified nanobodies were aliquoted and frozen in liquid nitrogen.

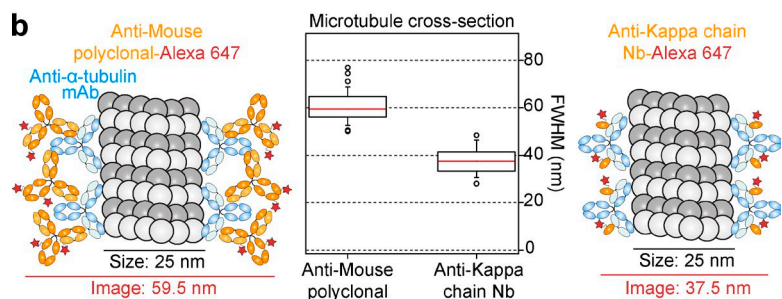
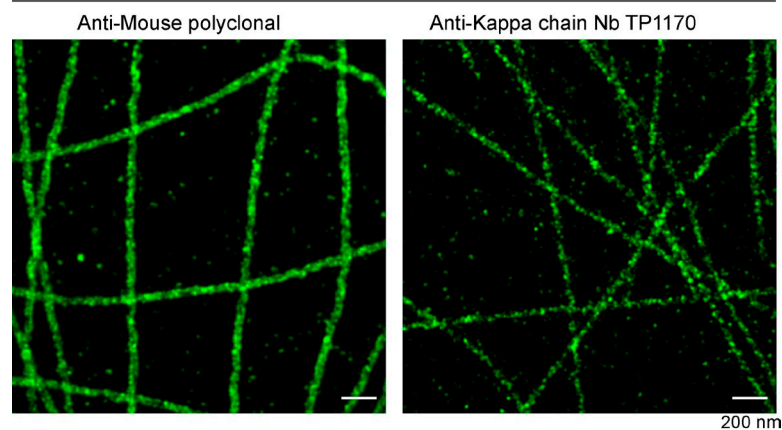
a STORM imaging of microtubules in BS-C-1 cells via:

Figure 6. STORM imaging with anti- κ chain nanobody TP1170. (a) BS-C-1 cells were stained with an anti- α tubulin monoclonal antibody (IgG1 κ) and detected with Alexa Fluor 647-labeled goat anti-mouse polyclonal antibody or Alexa Fluor 647-labeled anti-mouse κ chain nanobody TP1170. STORM images of the two samples show subdiffraction limit organization of the tubulin filaments. (b) To quantify the effect of the label size on the apparent width of the filaments in the STORM images, averaged cross-sectional profiles of straight segments of filaments from the two samples were measured. First, the two labeling approaches are illustrated on the left and right of the figure, showing the expected smaller width for the nanobody labeling case. In the middle, box plots illustrate the results of the width analysis (boxes indicate first and third quartiles of data values, whereas the red line indicates the median value; error bars indicate the 10th and 90th percentiles). In these measurements, the median width of the tubulin filaments decreased by a significant amount (from 59.5 to 37.5 nm) when stained with the anti-mouse κ chain nanobody TP1170.

Expression of bdNEDP1 protease from pDG02583

For expression of the previously described *bdNEDP1* protease (Frey and Görlich, 2014), we used here an optimized construct encoding a His14-MBP-*bdSUMO*-*bdNEDP1* fusion (pDG02583). The MBP-*bdSUMO* module enhances soluble expression. The plasmid was transformed into *E. coli* NEB express F'. An 80-ml preculture (TB medium containing 50 μ g/ml kanamycin) was grown at 28°C in a 5-liter flask overnight. The culture was then diluted with fresh medium to 700 ml. After 1-h growth at 25°C, protein expression was induced with 0.2 mM IPTG at OD₆₀₀ ~2.0 for 5 h. Harvested cells were resuspended in lysis buffer (50 mM Tris/HCl, pH 8.0, 300 mM NaCl, 25 mM imidazole/HCl, pH 7.5, 10 mM DTT, and 250 mM sucrose), lysed by sonication, and ultracentrifuged. The supernatant was bound to a Ni²⁺-chelate resin, the column was thoroughly washed, and the fusion was eluted with lysis buffer containing 500 mM imidazole. The eluate was then rebuffed to 50 mM Tris/HCl, pH 7.5, 300 mM NaCl, 250 mM sucrose, and 10 mM DTT. This yields a His14-tagged *bdNEDP1* version that can be used for in-solution digests of His14-*bdNEDD8*-nanobody fusions, followed by reverse Ni chromatography to remove tag and protease.

Alternatively, the protease can be used for on-column cleavage and thus for a direct production of tag-free nanobodies (Pleiner et al., 2015). This protocol requires prior removal of the His-tag from the protease. For this, we added 100 nM His14-*bdSEN1* protease and 0.2% Tween-80 to the imidazole-eluted His14-MBP-*bdSUMO*-*bdNEDP1* protease and incubated the mixture for 1 h at room temperature or overnight at 4°C. During this time, the buffer is exchanged for degassed 50 mM Tris/HCl, pH 8.0, 300 mM NaCl, and 10 mM DTT by either gel filtration on Sephadex G25 (e.g., on a PD-10 column) or dialysis. Any aggregates were removed by ultracentrifugation, and the sample was applied to reverse Ni chromatography, which captures the cleaved His14-MBP-*bdSUMO* tag, the added His14-tagged *bdSEN1* protease, and any Ni-binding contaminants from the initial bacterial lysate. The flow-through fraction was collected, and the combined pool was supplemented with 250 mM sucrose. The protease concentration was

determined by reading the 280-nm absorbance ($\epsilon_{280} = 28,000$ M/cm), and the tag-free protease was snap-frozen in small aliquots and stored at -80°C for further use. The reason for using NEDD8 as a protease module is that it greatly enhances the soluble expression of nanobodies (Pleiner et al., 2015). Moreover, *bdNEDP1* is a far more efficient protease than the still more commonly used Tev protease (Frey and Görlich, 2014), allowing complete substrate cleavage with nanomolar protease concentrations within only 1 h on ice.

Expression and purification of the His14-*bdSEN1* helper protease was described previously (Frey and Görlich, 2014). The expression construct (pSF1389) is also available through Addgene (ID 104962).

Site-specific fluorescent labeling of nanobodies with engineered cysteines

The fluorescent labeling of nanobodies with maleimide dyes was described in detail (Pleiner et al., 2015). In brief, stored nanobodies were thawed, and the buffer was exchanged again to maleimide-labeling buffer to remove the reducing agent, using either Illustra NAP-5 or PD-10 desalting columns. For a standard labeling reaction, 5–10 nmol nanobody was rapidly mixed with 1.2 \times molar excess of fluorescent dye per cysteine on the nanobody and incubated for 1.5 h on ice. Free dye was separated from labeled nanobody by buffer exchange to maleimide-labeling buffer on Illustra NAP-5 or PD-10 desalting columns. Quantitative labeling was quality controlled by calculating the degree of labeling. Fluorescently labeled nanobodies were always aliquoted, snap-frozen in liquid nitrogen, and stored at -80°C until further use.

Dot blot assay for anti-IgG nanobody specificity profiling

To profile the binding of anti-IgG nanobodies to different IgG subclasses and analyze their cross reaction to IgG from other species, a dot blot assay was performed. Nitrocellulose membrane was cut in strips, and different IgGs (500 ng for polyclonal total IgG, Fab, and Fc fragments; ~250 ng for monoclonal IgG in 1 μ l) were spotted. Strips were blocked with 4% milk (wt/vol) in 1 \times PBS for 30 min at room

temperature. Nanobodies were added at ~300 nM in 1 ml milk for 30 min. After washing two times with 1× PBS for 10 min each, bound nanobodies were detected at 488 nm in a fluorescence scanner (Starion FLA-9000; Fujifilm). The following IgGs were used: IgG1 κ mAb A225 (Cordes et al., 1995); IgG1 λ (#010-001-331; Rockland); IgG2a κ (02-6200; Thermo Fisher Scientific); IgG2b κ (02-6300; Thermo Fisher Scientific); IgG3 κ (401302; BioLegend); polyclonal IgG Fab fragments (010-0105; Rockland); and polyclonal IgG Fc fragments (31205; Thermo Fisher Scientific). Polyclonal IgG of the following species were used: rabbit (made in-house, affinity-purified from serum); mouse (I8765); rat (I4131); goat (I5256); sheep (I5131); human (I4506; all Sigma-Aldrich); and guinea pig (CR4-10; Sino Biological).

Native isolation of IgG with anti-IgG nanobodies

Polyclonal rabbit IgG from serum or mouse mAbs from hybridoma cell culture supernatant were isolated natively with anti-IgG nanobodies. For this, 0.3 nmol biotinylated nanobodies carrying an N-terminal His₁₄-Biotin acceptor peptide-(GlySer)₉-SUMOStar-(GlySer)₉-tag were immobilized on 1 mg magnetic Dynabeads MyOne Streptavidin T1 (Thermo Fisher Scientific). Excess biotin binding sites were quenched with biotin-PEG-COOH (PEG1053; Iris Biotech). The beads were incubated with 1 ml precleared (10 min, 16,000 g at 4°C) serum or hybridoma supernatant for 30 min at 4°C. After washing two times with wash buffer (50 mM Tris/HCl and 300 mM NaCl), nanobody-bound IgG was eluted by addition of 50 µl of 0.5-µM SUMOStar protease (Liu et al., 2008) in wash buffer for 20 min on ice. An aliquot of the eluate was then analyzed by SDS-PAGE and Coomassie staining.

Western blotting

Bacteriophage protein III was detected with a mouse anti-pIII IgG2a mAb (#E8033S; New England Biolabs). Mouse mAbs used for detection of human proteins in HeLa cell lysate were as follows: anti-Skp1 (clone H-6, sc-5281; Santa Cruz Biotechnology), anti-α-tubulin (clone DM1A, T6199; Sigma-Aldrich), and anti-Histone H3 (clone 96C10, 3638; Cell Signaling Technologies). Polyclonal goat anti-mouse IgG coupled to IRDye 800CW (925-32210; LI-COR Biosciences) was used to detect primary mouse antibodies at a dilution of 1:1,340 (5 nM). Polyclonal rabbit antibodies against *Xenopus* nucleoporins Nup98, Nup93, Nup54, Nup88, and Nup107 were prepared in the laboratory (Hülsmann et al., 2012). Polyclonal goat anti-rabbit IgG coupled to IRDye 800CW (925-32211; LI-COR Biosciences) was used to detect primary rabbit antibodies at the lowest suggested dilution of 1:5,000. Anti-mouse IgG1 Fab nanobody TP886 (5 nM), anti-mouse IgG1 Fc nanobody TP1107 (5 nM), and anti-rabbit IgG nanobody TP897 (10 nM) were labeled with a single IRDye 800CW maleimide (929-80020; LI-COR Biosciences) via a C-terminal cysteine and used at the indicated concentrations in 4% (wt/vol) milk in 1× PBS.

Polyclonal goat anti-mouse-HRP conjugate was obtained from DakoCytomation and used at 1:1,000 dilution (5 nM). Anti-mouse IgG1 Fc nanobody TP1107 was conjugated to maleimide-activated HRP (31485; Thermo Fisher Scientific) via a C-terminal cysteine by mixing both in equimolar amounts and incubating for 1 h at room temperature. The conjugate was used at 5 nM in 4% (wt/vol) milk in 1× PBS. The ECL solution was made in-house and contained 5 mM Luminol (A4685; Sigma-Aldrich), 0.81 mM 4-iodophenylboronic acid (471933; Sigma-Aldrich), and 5 mM of freshly added H₂O₂ in 0.1 M Tris/HCl, pH 8.8.

Amplex Ultra Red assay

APEX2 was derived from pTRC-APEX2 (plasmid 72558; Addgene), which was a gift from A.Y. Ting (Stanford University, Stanford, CA; Lam et al., 2015). The anti-mouse IgG1 Fc nanobody TP1107-

APEX2 fusion was expressed from pTP1135 with an N-terminal His₁₄-bdNEDD8-tag in *E. coli* NEB express F' (New England Biolabs) for 6 h at 25°C in the presence of 1 mM heme precursor 5-aminolevulinic acid (A3785; Sigma-Aldrich). After lysis, the protein was purified by nickel chelate affinity chromatography and eluted by cleavage with 500 nM bdNEDP1 protease (Frey and Görlich, 2014) in 100 mM potassium phosphate, pH 7.5, 150 mM NaCl, and 250 mM sucrose. The final assay mix contained 160 µM Amplex Ultra Red and 160 µM H₂O₂ in either 100 mM citrate, pH 6.6, and 150 mM NaCl (optimal pH for APEX2) or 100 mM potassium phosphate, pH 6.0, and 150 mM NaCl (optimal pH for HRP). 50 µl of this mix was used per reaction. Anti-mouse IgG1 Fc nanobody TP1107-APEX2 was titrated from 167 nM to 470 fM in a 1.8-fold dilution series, and 2 µl of each dilution was added to 50 µl reaction mix in triplicate. HRP (31490; Thermo Fisher Scientific) was titrated from 31 nM to 5 fM in a 2.4-fold dilution series, and 2 µl per dilution was added to 50 µl reaction mix in triplicate. The 96-well plate containing these reactions was incubated at room temperature for 30 min, and resorufin fluorescence was measured at 590 nm (530-nm excitation) in a Bio-Tek Synergy HT Multi-Detection Microplate Reader (BioTek Instruments).

Immunofluorescence

HeLa cells grown on glass coverslips were fixed for 10 min at room temperature with 3% (wt/vol) PFA and washed two times with 1× PBS for 5 min each. Residual PFA was quenched by incubation with 50 mM NH₄Cl in 1× PBS for 5 min. After two washes with 1× PBS for 5 min each, the cells were permeabilized with 0.3% (vol/vol) Triton X-100 for 3 min. Then the cells were washed three times quickly with 1× PBS and blocked for 30 min with 1% (wt/vol) BSA in 1× PBS (blocking buffer). After blocking, the coverslips were stained with primary antibody, which was diluted in blocking buffer, in a humid chamber for 1 h at room temperature. The coverslips were then washed two times in 1× PBS for 15 min each and added again to a humid chamber for incubation with secondary antibody or anti-IgG nanobody diluted in blocking buffer. Afterward, the cells were washed two times in 1× PBS for 15 min each, and the coverslips were mounted with Slow Fade Gold (Thermo Fisher Scientific) for imaging on a TCS SP5 confocal microscope equipped with hybrid detectors (Leica).

For methanol fixation, the cells were incubated with -20°C-cooled methanol for 6 min at room temperature, washed two times in 1× PBS for 5 min each, and blocked in blocking buffer. The staining was performed as described in the previous paragraph.

Antibodies for immunofluorescence

The following rabbit antibodies were used for immunofluorescence on HeLa cells: anti-Lap2 polyclonal antibody (1:100 dilution; 14651-1-AP; Proteintech); anti-Ki-67 mAb clone D3B5 (1:200 dilution; 9129; Cell Signaling Technologies). The following mouse mAbs were used for immunofluorescence on HeLa cells: anti-Vimentin mAb clone V9 (1:10 dilution of hybridoma supernatant; gift of M. Osborn, Max Planck Institute for Biophysical Chemistry, Göttingen, Germany); anti-Ki-67 mAb clone B56 (1:50 dilution; 556003; BD Biosciences); anti-TPR mAb 203-37 (1:500 dilution; Matritech; Cordes et al., 1997); anti-cytochrome *c* mAb clone 6H2.B4 (1:50 dilution; 556432; BD Biosciences); anti-lamin A/C mAb clone 4C11 (1:50 dilution; 4777T; Cell Signaling Technologies); and anti-CD44 mAb clone 156-3C11 (1:200 dilution; 3570T; Cell Signaling Technologies). Polyclonal goat anti-rabbit IgG (111-545-003) and goat anti-mouse IgG (115-545-003; Jackson ImmunoResearch) coupled to Alexa Fluor 488 were used as secondary antibodies at 1:150 dilution (~33 nM). Anti-IgG nanobodies were labeled with maleimide Alexa Fluor dyes at engineered surface cysteines (Pleiner et al., 2015) and used at 20 nM. The nanobodies used had the

following degrees of labeling: TP886–Alexa Fluor 488 = 1.9, TP1107–Alexa Fluor 488 = 2.7, TP1107–Alexa Fluor 647 = 2.2, TP1129–Alexa Fluor 488 = 2.5, TP1129–Alexa Fluor 568 = 2.0, TP1079–Alexa Fluor 488 = 2.2, TP1170–Alexa Fluor 488 = 2.5, TP1170–Alexa Fluor 647 = 2.3, and TP897–Alexa Fluor 488 = 2.2.

STORM imaging of microtubules in BS-C-1 cells

BS-C-1 cells (CCL-26; ATC–) were stained with an anti- α tubulin monoclonal antibody (1:200 dilution, T6074; Sigma-Aldrich) after PFA fixation as described in the Immunofluorescence section for HeLa cells. STORM imaging was performed using a custom-built microscope, similar to what has been described previously (Bates et al., 2012). In brief, 642 nm laser light was used to illuminate the sample, and fluorescence was detected with an EMCCD camera (Andor Ixon DU860), after filtering with a bandpass filter (ET700/75; Chroma Technologies). Raw STORM data were analyzed with custom-written software, and STORM images of each sample were rendered using summed Gaussian functions. For calculation of the cross-section histograms, multiple straight segments of tubulin filaments were selected from the STORM images. For each straight filament segment, a line was laid over the segment to define the filament axis. Next, a set of rectangular regions of interest (ROIs) was created, aligned with the segment and spanning the cross section of the filament. The ROI length was set equal to the segment length and a user-selectable ROI width, which was chosen to be 5 nm for this analysis (the bin width). By counting the number of localizations falling within each ROI, a histogram corresponding to the cross-sectional profile of the STORM image of a filament, averaged along the segment length, was generated. To measure the width of the cross section, a Gaussian function was fitted to the histogram, and the full width at half-maximum was calculated. The distribution of measured filament widths is shown in Fig. 6 b.

Online supplemental material

Table S1 lists anti-IgG nanobody protein sequences. Fig. S1 shows species cross reactivity profiling and native target IgG isolation. Fig. S2 shows anti-IgG nanobody conjugation to HRP and fusion to APEX2. Fig. S3 shows uncropped scans of the Western blots shown in Fig. 3. Fig. S4 shows immunofluorescence with anti-mouse IgG nanobodies.

Acknowledgments

We thank Ulrike Teichmann and Rolf Rümenapf for alpaca care and immunization; Jens Krull, Heinz-Jürgen Dehne, Gabriele Hawlitschek, Renate Rees, Jürgen Schünemann, and Tanja Gilat for excellent technical assistance; Philip Gunkel, Volker Cordes, and Mary Osborn for advice and antibodies (Max Planck Institute for Biophysical Chemistry, Göttingen, Germany); Bastian B. Hülsmann for anti-*Xenopus* Nup nanobodies and antigens (Max Planck Institute for Biophysical Chemistry, Göttingen, Germany); and Nataliia Naumenko and Trevor Huyton for critical reading of the manuscript.

We thank Max-Planck-Gesellschaft and the Deutsche Forschungsgemeinschaft (SFB1190) for funding this work.

T. Pleiner and D. Görlich are inventors on a European patent application encompassing the nanobodies described in this article.

The authors declare no further conflict of interest.

Author contributions: T. Pleiner: conception and design, acquisition of data, analysis and interpretation of data, drafting and revising the article; M. Bates: experiment design, acquisition of data, analysis and interpretation of data, drafting and revising the article; D. Görlich: conception and design, analysis and interpretation of data, drafting and revising the article.

Submitted: 28 September 2017

Revised: 29 November 2017

Accepted: 7 December 2017

References

- Arbabi Ghahroudi, M., A. Desmyter, L. Wyns, R. Hamers, and S. Muyldermans. 1997. Selection and identification of single domain antibody fragments from camel heavy-chain antibodies. *FEBS Lett.* 414:521–526. [https://doi.org/10.1016/S0014-5793\(97\)01062-4](https://doi.org/10.1016/S0014-5793(97)01062-4)
- Balzarotti, F., Y. Eilers, K.C. Gwosch, A.H. Gynnå, V. Westphal, F.D. Stefani, J. Elf, and S.W. Hell. 2017. Nanometer resolution imaging and tracking of fluorescent molecules with minimal photon fluxes. *Science.* 355:606–612. <https://doi.org/10.1126/science.aak9913>
- Bates, M., B. Huang, G.T. Dempsey, and X. Zhuang. 2007. Multicolor super-resolution imaging with photo-switchable fluorescent probes. *Science.* 317:1749–1753. <https://doi.org/10.1126/science.1146598>
- Bates, M., B. Huang, and X. Zhuang. 2008. Super-resolution microscopy by nanoscale localization of photo-switchable fluorescent probes. *Curr. Opin. Chem. Biol.* 12:505–514. <https://doi.org/10.1016/j.cbpa.2008.08.008>
- Bates, M., G.T. Dempsey, K.H. Chen, and X. Zhuang. 2012. Multicolor super-resolution fluorescence imaging via multi-parameter fluorophore detection. *ChemPhysChem.* 13:99–107. <https://doi.org/10.1002/cphc.201100735>
- Bradbury, A., and A. Plückthun. 2015a. Reproducibility: Standardize antibodies used in research. *Nature.* 518:27–29. <https://doi.org/10.1038/518027a>
- Bradbury, A.R., and A. Plückthun. 2015b. Getting to reproducible antibodies: The rationale for sequenced recombinant characterized reagents. *Protein Eng. Des. Sel.* 28:303–305. <https://doi.org/10.1093/protein/gzv051>
- Cordes, V.C., S. Reidenbach, and W.W. Franke. 1995. High content of a nuclear pore complex protein in cytoplasmic annulate lamellae of *Xenopus* oocytes. *Eur. J. Cell Biol.* 68:240–255.
- Cordes, V.C., S. Reidenbach, H.R. Rackwitz, and W.W. Franke. 1997. Identification of protein p270/Tpr as a constitutive component of the nuclear pore complex-attached intranuclear filaments. *J. Cell Biol.* 136:515–529. <https://doi.org/10.1083/jcb.136.3.515>
- Desmyter, A., S. Spinelli, A. Roussel, and C. Cambillau. 2015. Camelid nanobodies: Killing two birds with one stone. *Curr. Opin. Struct. Biol.* 32:1–8. <https://doi.org/10.1016/j.sbi.2015.01.001>
- Frey, S., and D. Görlich. 2014. A new set of highly efficient, tag-cleaving proteases for purifying recombinant proteins. *J. Chromatogr. A.* 1337:95–105. <https://doi.org/10.1016/j.chroma.2014.02.029>
- Göttfert, F., T. Pleiner, J. Heine, V. Westphal, D. Görlich, S.J. Sahl, and S.W. Hell. 2017. Strong signal increase in STED fluorescence microscopy by imaging regions of subdiffraction extent. *Proc. Natl. Acad. Sci. USA.* 114:2125–2130. <https://doi.org/10.1073/pnas.1621495114>
- Gray, A.C., S.S. Sidhu, P.C. Chandrasekera, C.F. Hendriksen, and C.A. Borrebaeck. 2016. Animal-friendly affinity reagents: Replacing the needle in the haystack. *Trends Biotechnol.* 34:960–969. <https://doi.org/10.1016/j.tibtech.2016.05.017>
- Hamers-Casterman, C., T. Atarhouch, S. Muyldermans, G. Robinson, C. Hamers, E.B. Songa, N. Bendahman, and R. Hamers. 1993. Naturally occurring antibodies devoid of light chains. *Nature.* 363:446–448. <https://doi.org/10.1038/363446a0>
- Helma, J., M.C. Cardoso, S. Muyldermans, and H. Leonhardt. 2015. Nanobodies and recombinant binders in cell biology. *J. Cell Biol.* 209:633–644. <https://doi.org/10.1083/jcb.201409074>
- Huang, B., H. Babcock, and X. Zhuang. 2010. Breaking the diffraction barrier: Super-resolution imaging of cells. *Cell.* 143:1047–1058. <https://doi.org/10.1016/j.cell.2010.12.002>
- Huang, F., G. Sirinakis, E.S. Allgeyer, L.K. Schroeder, W.C. Duim, E.B. Kromann, T. Phan, F.E. Rivera-Molina, J.R. Myers, I. Irnov, et al. 2016. Ultra-high resolution 3D imaging of whole cells. *Cell.* 166:1028–1040. <https://doi.org/10.1016/j.cell.2016.06.016>
- Hülsmann, B.B., A.A. Labokha, and D. Görlich. 2012. The permeability of reconstituted nuclear pores provides direct evidence for the selective phase model. *Cell.* 150:738–751. <https://doi.org/10.1016/j.cell.2012.07.019>
- Kijanka, M., B. Dorresteyn, S. Oliveira, and P.M. van Bergen in Henegouwen. 2015. Nanobody-based cancer therapy of solid tumors. *Nanomedicine (Lond.)*. 10:161–174. <https://doi.org/10.2217/nnm.14.178>
- Krainer, F.W., and A. Glieder. 2015. An updated view on horseradish peroxidases: Recombinant production and biotechnological applications. *Appl. Microbiol. Biotechnol.* 99:1611–1625. <https://doi.org/10.1007/s00253-014-6346-7>

- Lam, S.S., J.D. Martell, K.J. Kamer, T.J. Deerinck, M.H. Ellisman, V.K. Mootha, and A.Y. Ting. 2015. Directed evolution of APEX2 for electron microscopy and proximity labeling. *Nat. Methods*. 12:51–54. <https://doi.org/10.1038/nmeth.3179>
- Liu, L., J. Spurrier, T.R. Butt, and J.E. Strickler. 2008. Enhanced protein expression in the baculovirus/insect cell system using engineered SUMO fusions. *Protein Expr. Purif.* 62:21–28. <https://doi.org/10.1016/j.pep.2008.07.010>
- Martell, J.D., T.J. Deerinck, Y. Sancak, T.L. Poulos, V.K. Mootha, G.E. Sosinsky, M.H. Ellisman, and A.Y. Ting. 2012. Engineered ascorbate peroxidase as a genetically encoded reporter for electron microscopy. *Nat. Biotechnol.* 30:1143–1148. <https://doi.org/10.1038/nbt.2375>
- Marx, V. 2013. Calling the next generation of affinity reagents. *Nat. Methods*. 10:829–833. <https://doi.org/10.1038/nmeth.2607>
- McMahon, C., A.S. Baier, S. Zheng, R. Pascolutti, J.X. Ong, S.C. Erlandson, D. Hilger, A.M. Ring, A. Manglik, and A.C. Kruse. 2017. Platform for rapid nanobody discovery in vitro. *bioRxiv*. <https://doi.org/10.1101/151043>
- Moutel, S., N. Bery, V. Bernard, L. Keller, E. Lemesre, A. de Marco, L. Ligat, J.C. Rain, G. Favre, A. Olichon, and F. Perez. 2016. NaLi-H1: A universal synthetic library of humanized nanobodies providing highly functional antibodies and intrabodies. *eLife*. 5:e16228. <https://doi.org/10.7554/eLife.16228>
- Muyldermans, S. 2013. Nanobodies: Natural single-domain antibodies. *Annu. Rev. Biochem.* 82:775–797. <https://doi.org/10.1146/annurev-biochem-063011-092449>
- Pleiner, T., M. Bates, S. Trakhanov, C.T. Lee, J.E. Schliep, H. Chug, M. Böhning, H. Stark, H. Urlaub, and D. Görlich. 2015. Nanobodies: Site-specific labeling for super-resolution imaging, rapid epitope-mapping and native protein complex isolation. *eLife*. 4:e11349. <https://doi.org/10.7554/eLife.11349>
- Reardon, S. 2016. US government issues historic \$3.5-million fine over animal welfare. *Nature News*. May 20. <https://doi.org/10.1038/nature.2016.19958>
- Ries, J., C. Kaplan, E. Platonova, H. Eghlidi, and H. Ewers. 2012. A simple, versatile method for GFP-based super-resolution microscopy via nanobodies. *Nat. Methods*. 9:582–584. <https://doi.org/10.1038/nmeth.1991>
- Rust, M.J., M. Bates, and X. Zhuang. 2006. Sub-diffraction-limit imaging by stochastic optical reconstruction microscopy (STORM). *Nat. Methods*. 3:793–795. <https://doi.org/10.1038/nmeth929>
- Sahl, S.J., S.W. Hell, and S. Jakobs. 2017. Fluorescence nanoscopy in cell biology. *Nat. Rev. Mol. Cell Biol.* 18:685–701. <https://doi.org/10.1038/nrm.2017.71>
- Shen, H. 2013. Discovery of goat facility adds to antibody provider's woes. *Nature News*. Jan 14. <https://doi.org/10.1038/nature.2013.12203>
- Szymborska, A., A. de Marco, N. Daigle, V.C. Cordes, J.A. Briggs, and J. Ellenberg. 2013. Nuclear pore scaffold structure analyzed by super-resolution microscopy and particle averaging. *Science*. 341:655–658. <https://doi.org/10.1126/science.1240672>
- Traenkle, B., and U. Rothbauer. 2017. Under the microscope: Single-domain antibodies for live-cell imaging and super-resolution microscopy. *Front. Immunol.* 8:1030. <https://doi.org/10.3389/fimmu.2017.01030>
- Van Bockstaele, F., J.B. Holz, and H. Revets. 2009. The development of nanobodies for therapeutic applications. *Curr. Opin. Investig. Drugs*. 10:1212–1224.
- Weber, K., P.C. Rathke, and M. Osborn. 1978. Cytoplasmic microtubular images in glutaraldehyde-fixed tissue culture cells by electron microscopy and by immunofluorescence microscopy. *Proc. Natl. Acad. Sci. USA*. 75:1820–1824. <https://doi.org/10.1073/pnas.75.4.1820>
- Xu, K., H.P. Babcock, and X. Zhuang. 2012. Dual-objective STORM reveals three-dimensional filament organization in the actin cytoskeleton. *Nat. Methods*. 9:185–188. <https://doi.org/10.1038/nmeth.1841>
- Zimmermann, I., P. Egloff, C. Hutter, P. Stohler, N. Bocquet, M. Hug, M. Siegrist, L. Svacha, J. Gera, and S. Gmuer. 2017. Synthetic single domain antibodies for the conformational trapping of membrane proteins. *bioRxiv*. <https://doi.org/10.1101/168559>